# **Chapter 8**

# Computational Studies of Mechanical Remodeling of Substrate Proteins by AAA+ Biological Nanomachines

Ruxandra I. Dima\* and George Stan\*

Department of Chemistry, University of Cincinnati, P. O. Box 210172, Cincinnati, Ohio 45221, United States

\*Email: ruxandra.dima@uc.edu. (R.I.D.)

\*Email: george.stan@uc.edu. (G.S.)

Biomechanical forces play a central role in the action of AAA+ (ATPases associated with various cellular activities) nanomachines to assist essential cellular processes such as protein degradation and microtubule severing. These nanomachines, which have a ring-shaped hexameric structure, exert a mechanical action on their substrates through a set of central channel loops. The loops grip parts of the substrate polypeptide chain and apply forces on the rest of the substrate. These stochastic forces arise from the cyclical axial motions of the loops. This review discusses our computational investigations, performed using coarse-grained or atomistic descriptions of biopolymeric molecules, into the mechanisms of two classes of AAA+ nanomachines that mediate these processes. In the degradation pathway, caseinolytic protease ATPases perform unfolding and threading actions on substrate proteins (SPs) to enable their degradation within the central peptidase chamber. Our studies reveal the dependence of remodeling mechanisms on SP topology and uncover the role of rotational diffusion of multidomain SPs in modulating the mechanical unfolding action. Microtubules are assemblies of biopolymers found in most eukaryotic cells, with homologs in eubacteria and archea. They have roles in all crucial cellular processes from mitosis to intracellular transport, and the maintenance of cell shape. Understanding how the dynamics of these biopolymers is modulated by the interactions with a large array of microtubule associated proteins, which results in microtubules being available when and where the cell requires, is an ongoing effort in cell biology. Here we present a review of our recent work in modeling the response of microtubule lattices to the proposed mechanisms of action of a specific class of microtubule associated proteins, the severing enzymes, which modulate microtubule dynamics by inducing filament cutting.

#### Introduction

Biological nanomachines in the AAA+ (ATPases associated with diverse cellular activities) superfamily utilize mechanical forces to assist diverse cellular mechanisms such as DNA replication, protein degradation, disassembly of toxic protein aggregates, severing of microtubules (MTs), or transporting cargo along MTs (1–3). These machines assemble in single– or double–ring hexamers that enclose a narrow central channel with a dynamic diameter of 1–2 nm (4–7). Catalytic activity is provided by one or two conserved nucleotide–binding domains (NBDs), or AAA domains, that power large–scale conformational transitions of individual subunits through ATP hydrolysis (8, 9). The hallmark mechanical action of the AAA+ machines involves gripping and applying force onto the substrate protein (SP) through a set of flexible loops, one in each NBD, that protrude into the central channel and undergo repetitive axial motions in nonconcerted allosteric cycles (10–14). These loops comprise a conserved G–aromatic–hydrophobic–G sequence motif, which allows a strong interaction with the SP and enables a "paddling" mechanism to promote force application in the axial direction (14, 15).

In this review, we focus on our recent results on the action of two classes of AAA+ machines, bacterial caseinolytic protease (Clp) ATPases that perform SP unfolding and translocation in the degradation pathway and severing enzymes (katanin or spastin), which are responsible for the severing of MTs. Our computational studies, performed at multiple length and time scales, yield diverse mechanical remodeling pathways associated with these processes resulting in extensive sampling of the conformational space of the polypeptide chains and of the polymeric assemblies. Statistical mechanical approaches used to analyze these results reveal detailed information about the reaction kinetics of SP unfolding and translocation, the coupling between mechanical pulling or pushing mediated by AAA+ machines and SP remodeling, and the effect of rotational diffusion of folded SP domains on the remodeling mechanism.

Clp machines, which assist protein degradation, are assembled through axial stacking of one or two ATPases, such as the single-ring ClpX or ClpY or the double-ring ClpA, and a central peptidase chamber, ClpP or ClpQ (5, 16-19). Recognition of diverse SPs through a short C-terminal peptide tag, such as the E. coli SsrA (20-23), or through an intrinsic sequence (24-26), unleashes the powerful mechanical unfolding mechanism mediated by the Clp ATPase that enables threading the polypeptide chain through the central pore and its ultimate fragmentation by the peptidase. Degradation rates are primarily dependent on the mechanical resistance of the SP near the point of force application rather than the global thermal stability of the folded domain (27, 28). In agreement with the local stability model, lower degradation rates are observed for dihydrofolate reductase (DHFR), which has a mechanically strong  $\beta$ -sheet terminal structure, than barnase, which has a softer  $\alpha$ -helical structure. In addition to the local topology, mechanical anisotropy of the SP renders the direction of force application an important factor in controlling the degradation rate. For example, the β-sheet of the 127 domain of titin may be unfolded through an unzipping mechanism by applying force in a softer mechanical direction perpendicular to the  $\beta$ -sheet registry or through shearing by a force in the stronger direction parallel to it. Single-molecule force spectroscopy experiments using Laser Optical Tweezers (LOT) or Atomic Force Microscopy (AFM) have provided valuable insight into the Clp-mediated mechanisms by probing a selective mechanical interface along the direction of N-C terminals (29-34). These experiments revealed that processive unfolding of multidomain SPs occurs through successive events of domain unraveling interspersed with dwell times. The unfolding pathways reflect the height of energy barriers encountered in mechanical pulling along the N-C direction and indicate a lower bound of ≈ 20 pN for the

loop–mediated force, corresponding to mechanical work  $\approx 5k_BT$ . Coordinated pulling by multiple loops within allosteric cycles was found to yield polypeptide translocation bursts of 1-4 nm.

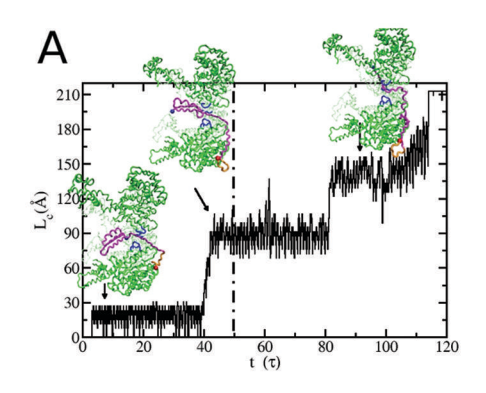
SP unfolding and translocation mechanisms have also been studied using computer simulations of model pores or coarse–grained descriptions of the Clp–SP system (35–38). To probe the coupling between the dynamic conformational changes of the Clp subunits and SP remodeling actions, we developed coarse-grained and atomistic simulations of SP unfolding and translocation in repetitive allosteric cycles (39-44). Our studies, using small model SPs, such as a four-helix bundle protein (HBP) and an  $\alpha/\beta$  protein, pinpointed the role of local SP topology in these mechanisms. We found that, whereas unfolding of both SPs is initiated at the tagged C-terminal, faster unfolding time scales are associated with weaker mechanical resistance near the terminal (39, 40). Our coarse-grained and atomistic simulations of Clp-mediated remodeling of single and tandem SPs comprising fusion I27 domains probed direction—dependent unfolding mechanisms. Our results revealed that the plasticity of Clp ATPase oligomer modulates SP unfolding by favoring the unzipping mechanism in the open pore configuration and the shearing mechanism in closed pore configurations (43). In atomistic simulations of allosteric Clp cycles, we found that the presence of multiple folded domains in a tandem SP strongly affects the rotational diffusion of folded domains through a crowding effect and results in branching of unfolding pathways due to sampling of multiple SP orientations (44). In additional simulations, we compare and contrast these mechanisms with those in a restrained geometry that mimics the single-molecule force spectroscopy setup. In accord with the experimental results, we find single unfolding pathways consistent with the mechanical interface along the N-C direction and weak effects due to the presence of multiple folded domains.

An important class of AAA+ machines is that of microtubule (MT)-severing enzymes, which use the energy from the ATP hydrolysis to break the MT lattice, resulting in formation of blunt ends, during cellular processes such as mitosis and meiosis (45–47). MTs, the longest and most rigid cytoskeletal filaments, are polymeric assemblies of non-covalently linked subunits called tubulin dimers, which consist of one  $\alpha$  and one  $\beta$  monomer. The subunits are arranged in protofilaments (PFs), which are rungs of longitudinally-connected tubulin dimers. The standard cellular MT filament is composed of 13 PFs connected laterally and arranged in a helical fashion resulting in a B-lattice characterized by the fact that each like monomer ( $\alpha$  and, respectively,  $\beta$ ) from a PF forms lateral contacts with the neighboring like monomers from its two adjacent PFs. This rule applies to all lateral interfaces between PFs, with the exception of the interface between PFs 1 and 13 which is an A-lattice where the  $\beta$  monomer from one PF is in lateral contact with the  $\alpha$  monomer from its neighbor and vice-versa. This lateral interface is called the seam. Three classes of MTsevering enzymes are known: katanin, spastin, and fidgetin (48, 49). While they are functional only in oligomeric form, most likely as a hexamer, reports from the literature indicate that the hexamer forms only in the presence of ATP and possibly a minimal substrate peptide (48). The first structure of a severing enzyme was one for spastin (PDB code 3B9P) (50) and showed that the AAA ATPase domain contains the canonical  $\alpha/\beta$  NBD embraced by two helices, and a smaller four-helix bundle domain (HBD). Moreover, the AAA domain is linked to an N-terminal domain consisting of a three-helix bundle (PDB code 2RPA) (51) that binds MTs with low affinity (52). High-resolution structures for the hexameric states of katanin and spastin have only recently been solved using cryo-EM (53-57). The authors found populations corresponding to two main states: one helical (spiral) where all protomers are ATP-bound, and another ring where one protomer has no density for a nucleotide. All structures show that the hexamer has a central pore lined by 3 pore loops important for MT-severing, which is flanked by helices with roles in the ATPase activity. While the way the

hexameric enzyme gets oriented on a MT lattice is unknown, experiments showed that the acidic carboxy-terminal end (CTT) of tubulin subunits binds to the central pore of the enzyme (58). This interaction is functionally-relevant as for both katanin and and spastin, the removal of the CTT through enzymatic digestion completely inhibits their ability to sever (50, 58). Moreover, several groups showed that defects in the MT lattice may be important to initiate severing (59) as severing motors have higher affinity for defect sites within the filament (60) such as missing subunits, dislocations (61, 62), and post-translational modifications. These findings indicate that the mechanical and dynamic nature of MTs are directly linked with the nanoscale structural integrity of the filament.

A major unknown is the severing mechanism. The only aspect that is known for certain is that it consists of the application of forces by the hexameric form of the severing enzyme on the MT lattice (63). There are two main proposed mechanisms in the literature (64). The first mechanism is the "unfoldase" and it is based on the typical mechanism that other AAA+ machines such as ClpX use to unfold their small protein substrates (29). The idea is that the severing enzyme tears out dimers from the lattice by using the mechanical work of sequential ATP hydrolysis to pull and thread the tubulin peptide chain through the central pore of the hexameric complex (53, 58, 64, 65). Importantly, the degree of unraveling in the tubulin monomers must be minimal as the severed subunits have been shown to reincorporate into nearby MT structures (66). Support for the unfoldase mechanism was recently provided by the finding of a helical staircase arrangement of pore loops in the highest resolution structures of the spiral states of the hexameric katanin and spastin, which suggests a hand-over-hand passing from one severing enzyme protomer to the next of the portion of a tubulin chain located inside the enzyme (56, 57). The second proposed mechanism is the "wedge". In this case, a severing enzyme bound to the CTT holds it rigidly within the pore of its hexameric form while the main mechanical action corresponds to a pushing force on the MT lumen resulting in the destabilization and ultimately the cutting of the MT lattice structure (50, 53, 64). In summary, at this time there is no agreement on many fundamental aspects of MT severing such as the orientation of the hexameric states of the enzymes on MTs, the degree of cooperativity between enzymes, the amplitude and the direction of the forces required to cut the MT lattice, and the molecular steps responsible for severing (64, 67, 68). Also, despite the biochemical evidence, there are no direct mechanical measurements of MTs during the process of severing. Such mechanical measurements would need to use force monitoring in some way (68). The only available experimental results are those from AFM indentation experiments on bare MT filaments (69-72).

Our efforts have been directed towards addressing a number of these challenging MT severing aspects: the role of lattice defects, and the molecular-level steps that would correspond to the two proposed severing mechanisms reviewed above. Due to the lack of direct experimental measurements, we focused on in silico measurements of the dynamics of lattice breaking under forces. This allows us to direct forces to push and pull in specific locations on the lattice. In our work we employed the self-organizing polymer (SOP) model (73), coupled with Brownian dynamics, to follow the removal of tubulin dimers from different MT lattices (defect-free and with defects). To probe the unfoldase mechanism, we applied constant-loading rate pulling forces to select regions of an MT filament (74). To probe the wedge mechanism, we followed the bending and destruction of MTs under the action of indentation forces applied akin to AFM studies (75, 76). In both cases, we compared and contrasted our distributions of MT lattice bending and breaking angles to experimental results from in vitro severing experiments.



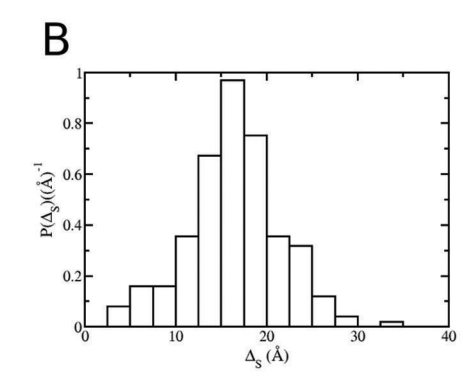


Figure 1. Translocation of a model  $\alpha/\beta$  protein mediated by the allosteric ClpY pore. (A) Stepped transitions are observed in the contour length of the translocated polypeptide chain as a function of time. Harmonic restraints are applied in the distal region after  $t=50\,\tau$ . (B) Translocated segment during each cycle has an end–to–end extension ( $\Delta_S$ ) commensurate with the axial motion of 1–3 central channel loops.

Reproduced under Creative Commons Attribution (CC BY) open license from reference (42).

#### **Results and Discussion**

# Coarse-Grained Simulations of Model Substrate Proteins Highlight Topology-Dependent Remodeling Mechanisms

Large time and length scales associated with the action of AAA+ machines represent major challenges for computational studies of these systems. To overcome such requirements, we first studied mechanisms involving model proteins, which can be designed according to specific requirements. Considering SPs with diverse topology and relatively simple energy landscapes facilitates access to the relevant time scales to probe mechanisms such as the local stability hypothesis. To this end, we considered model proteins which have either  $\alpha$ -helical or combined  $\alpha$ helical and  $\beta$ -sheet ( $\alpha/\beta$ ) structure. We focused on a four-helix bundle protein (HBP), designed by the DeGrado group (77), and an  $\alpha/\beta$  protein, which has the same fold as the B1 domain of proteins L and G, comprising N- and C-terminal  $\beta$ -hairpins that flank an internal  $\alpha$ -helix. The mechanical resistance of these protein folds reflects the stabilization mechanisms of each topology. The  $\alpha$ -helical structure has weaker mechanical resistance given its stabilization by van der Waals interactions between helical regions, whereas the  $\alpha/\beta$  protein has stronger mechanical resistance given its stabilizing hydrogen bond network. We probed the bulk unfolding mechanisms of each of these model SPs by using an approach that mimics single-molecule force spectroscopy experiments through application of mechanical force at the C-terminal, along the N-C direction, while maintaining the N-terminal at a fixed position (see Methods). For both SPs, we found that unfolding proceeds along multiple pathways (39, 42). In the HBP case, the major pathway, which occurs in 75% of simulation trajectories, corresponds to unfolding initiated through removal of the N–terminal helix, while the minor pathway corresponds to the unfolding initiated at the pulled C-terminal (39). In the  $\alpha/\beta$  protein case, the major pathway, which occurs in 45% of trajectories, corresponds to unfolding of the N-terminal hairpin, the secondary pathway, which occurs in 41% of trajectories, corresponds to unfolding of the C-terminal hairpin first (42), and the tertiary pathway corresponds to simultaneous unfolding of both hairpins.

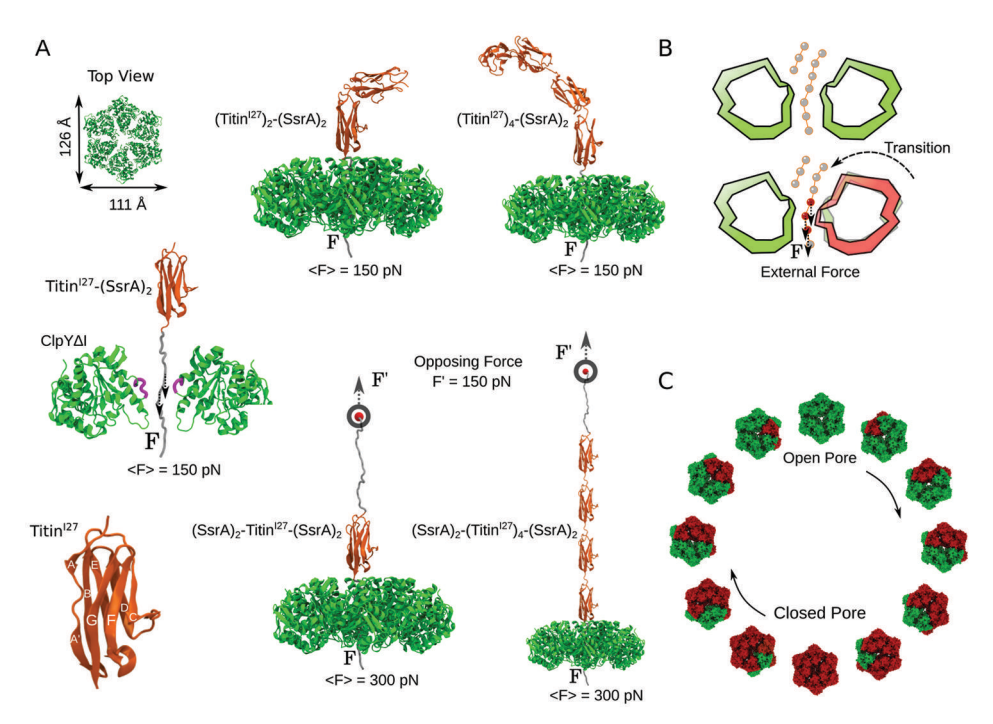


Figure 2. Simulations of ClpYΔI-mediated remodeling of I27 tandem SPs. (A). Unrestrained (top panels) or restrained (bottom panels) multidomain SPs with 1, 2, or 4 I27 domains (orange) and (SsrA)<sub>2</sub> peptides (gray) in allosteric cycles of ClpYΔI (green and gray). Conserved central channel loops are shown in purple (orange). An axial external force is applied on amino acids transiently located within the pore and an opposing force is applied onto the N-terminal in the restrained simulations. (B) Schematic representation of conformational transitions of ClpY subunits between "open" (green) and "closed" (red) pore configuration. (C) The ClpY cycle is described using 12 clockwise subunit conformational transitions. Each subunit undergoes a transition between its open (green) and closed (red) pore configuration. Reproduced with permission from reference (44). Copyright 2019 American Chemical Society.

Next, we performed coarse-grained simulations that probed unfolding of these model SPs in repetitive cycles of the ClpY ATPase (see Methods). Our results revealed distinct pathways of Clpmediated unfolding compared with those observed in bulk unfolding. For HBP, we found that unfolding requires removal of the C-terminal helix as an obligatory initial step. Binding of the resulting three–helix bundle fragment to the auxiliary I–domains helps to stabilize this folded HBP fragment until further unfolding occurs either prior to or simultaneous with translocation (39). For the  $\alpha/\beta$  protein, the reaction kinetics comprises complex pathways that may involve simultaneous unfolding and translocation or several unfolding events prior to translocation (42). In both cases, unfolding is initiated at the C-terminal, where the mechanical force is applied due to pulling by the ClpY channel loops. Translocation of both SPs involves sharp stepped transitions which indicates that ClpY uses a power stroke mechanism to process the polypeptide chain. In accord with this observation, we find that translocation involves collaboration of 1-3 ClpY loops within an ATPase cycle through successive SP gripping and force application. This intra-ring allosteric cooperativity results in translocation of polypeptide segments with end-to-end extensions of 1-3 nm, commensurate with the multiple 1 nm excursions of individual loops along the channel axis (Figure 1). Simulation results are in very good agreement with experimental studies that indicate discrete translocation steps of 1-4 nm in GFP degradation mediated by the ClpX machine (13, 31, 32). In addition to these similar SP remodeling actions, we found topology–dependent mechanisms that occur due to distinct SP mechanical resistance near the C–terminal and the direction of force application. In particular, HBP unfolding of occurs on a fast time scale that reflects the weak stabilizing contacts of the C–terminal helix in the bundle. By contrast,  $\alpha/\beta$  SP unfolding involves longer time scales consistent with the hydrogen–bonded network stabilizing the C–terminal hairpin. Whereas initial HBP unfolding involves removal of the C–terminal helix through a single mechanism, unfolding of the C–terminal hairpin of the  $\alpha/\beta$  SP occurs through either shearing or unzipping mechanisms. The bifurcated pathways of the  $\alpha/\beta$  SP are consistent with the application of mechanical force along different directions of mechanical resistance. As a result of the distinct unfolding properties of these SPs, translocation represents the rate–limiting step of degradation of HBP whereas unfolding is the rate-limiting step for degradation of the  $\alpha/\beta$  protein. Overall, our results are consistent with experimental observations that indicate processive degradation of SPs initiated at the tagged polypeptide terminal and with the local stability hypothesis that suggests higher degradation rates of HBP due to the weaker mechanical resistance near its C–terminal.

# Multiscale Modeling of I27 Remodeling Reveals Role of Interactions with the Clp ATPase Surface and the Effect of Multidomain SPs

To elucidate the role of mechanical anisotropy in Clp-mediated remodeling of SPs, we performed coarse-grained simulations of threading of the I27 domain of titin through the ATPase pore (see Methods) (43). The I27 domain has a  $\beta$ -sheet structure that is stabilized by the "mechanical clamp" involving hydrogen bonds between the N- and C-terminal A'-G strands, therefore unfolding along the N–C direction, which is aligned with the  $\beta$ -sheet registry, requires cooperative removal of these contacts. Thus, the N-C direction represents a strong mechanical interface. Our simulations probed the unfolding and translocation of the I27 monomer through the channel of ClpY $\Delta$ I, which lacks the auxiliary I domain, in open and partially closed pore configurations that model intermediate conformations in the nonconcerted ATPase allosteric cycle. In these simulations we considered SP unfolding both in the restrained geometry in which the C-terminal of the SP is engaged by the ATPase whereas the N-terminal is restrained through an opposing force, as in single-molecule force spectroscopy experiments, and in an unrestrained geometry, as in the in vivo degradation process. We found that, in the unrestrained geometry, SP unfolding occurs through an unzipping mechanism in the open pore configurations as the A'-G interface is oriented perpendicular to the ClpY $\Delta$ I axis and mechanical force is applied along a direction of weak resistance. A shearing mechanism is identified in the partially closed pore configuration as the A'-G interface is nearly aligned with the Clp axis and force is applied along a direction of strong mechanical resistance. In the restrained geometry, SP unfolding involves only the shearing mechanism as the mechanical force is applied in the direction parallel to the A'-G interface. Given the large heterogeneity of the Clp ATPase surface resulting from nonconcerted subunit motions, we propose that Clp plasticity modulates these direction-dependent SP remodeling mechanisms.

Experimental studies of degradation of fusion proteins comprising multiple folded domains indicated the release of partially degraded species containing a subset of the domains (78). To understand the degradation mechanisms of multidomain SPs, we performed atomistic simulations of unfolding and translocation of tandem SPs consisting of one, two or four I27 domains in repetitive cycles of ClpY $\Delta$ I (see Methods and Figure 2) (44). In accord with our prior coarse–grained results discussed above, the atomistic simulations revealed that monomeric SPs unfold on a fast time scale

through a single pathway corresponding to unzipping the A'-G interface. We found that dynamic conformational changes of the ClpY pore during the allosteric cycles coupled with the rotational flexibility of the I27 monomer allow the SP orientation such that pulling is effected along the soft mechanical direction (Figure 3). By contrast, unfolding of multimeric SPs occurs on significantly longer time scales and through branched pathways that use either unzipping, when force is applied along a soft mechanical direction, or shearing mechanisms, when force is applied along the strong mechanical direction. These distinct mechanisms arise from hindered rotational diffusion of the C–terminal I27 domain in tandem SPs as the presence of multiple folded domain induces a crowding effect. In the restrained geometry, a single unfolding pathway was identified for both monomeric and tetrameric SPs, as the mechanical tension along the N–C direction precludes the crowding of folded domains.

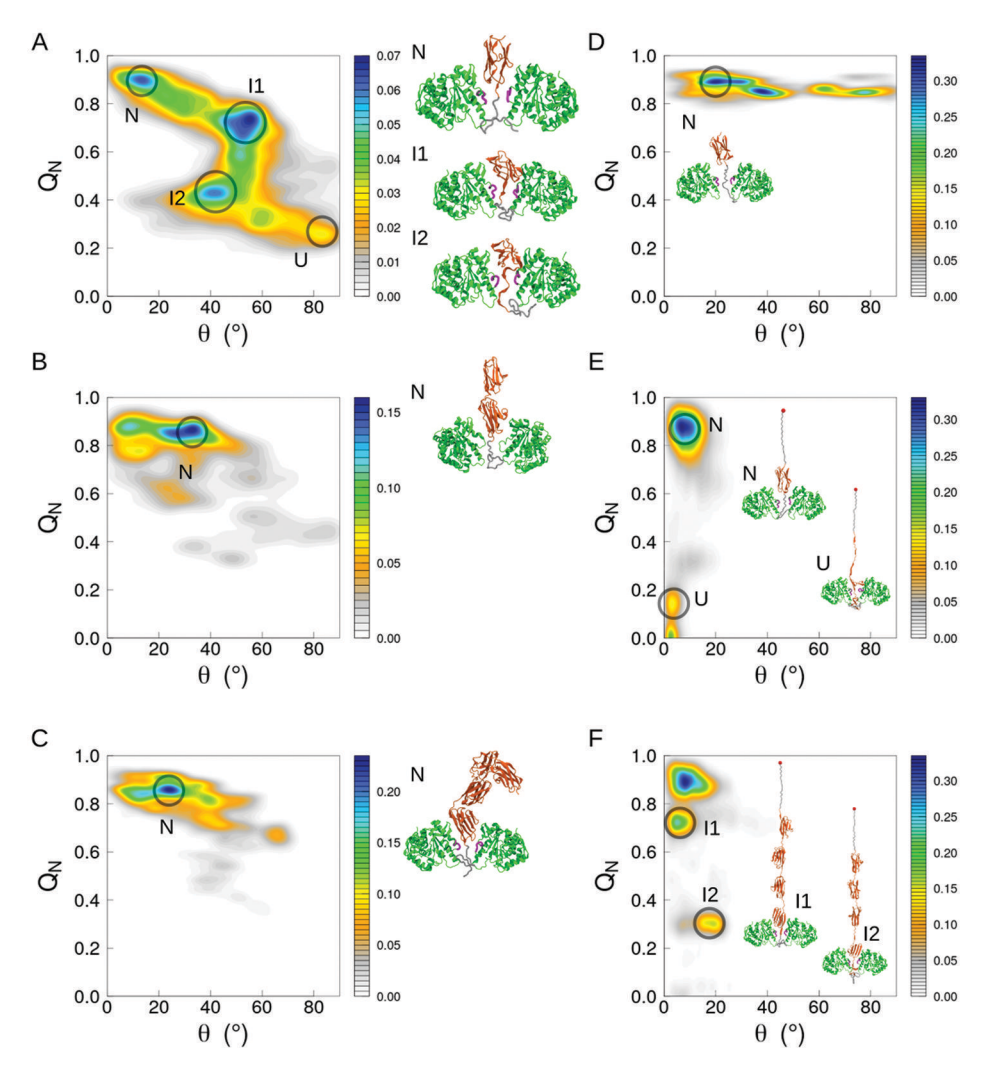


Figure 3. Mechanisms of direction–dependent unfolding of tandem SPs mediated by  $ClpY\Delta I$ . Probability density map of unfolding  $(Q_N)$  and orientation  $(\theta)$  of unrestrained (A) monomeric (B) dimeric and (C) tetrameric SPs in allosteric cycles of  $ClpY\Delta I$ ; (D) unrestrained monomeric SP for the non-allosteric  $ClpY\Delta I$ ; Restrained (E) monomeric and (F) tetrameric SPs in allosteric cycles of  $ClpY\Delta I$ . Reproduced with permission from reference (44). Copyright 2019 American Chemical Society.

Coarse-Grained Modeling of the Mechanical Response of Microtubules Highlights the Specificity of the Action of Severing Enzymes, a Class of AAA+ Proteins

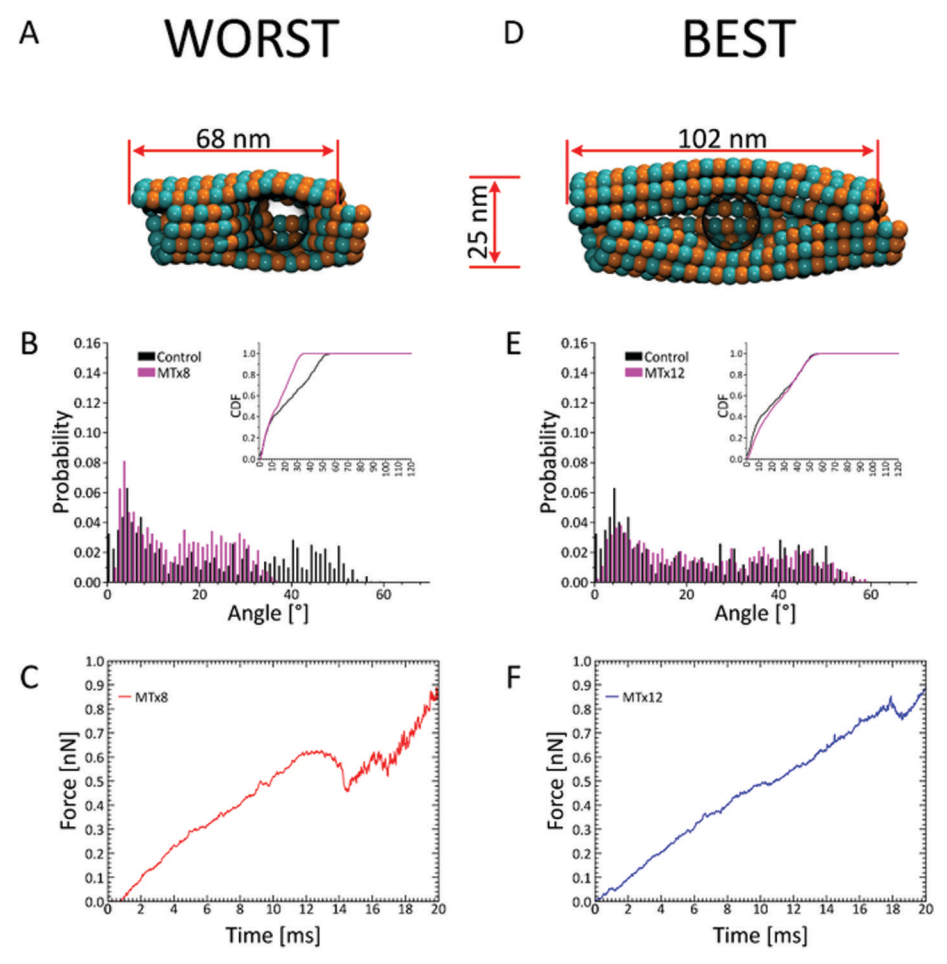


Figure 4. Results of molecular indentation studies of MT lattices. (A) Final stage of indentation on a MT lattice with 8 dimers in each PF and the ends of the lattice kept fixed. The cantilever-like sphere is represented through the black circle and the dimensions (filament length and diameter) are listed. (B) the distribution of bending angles from this type of simulation (magenta) versus angles obtained during in vitro severing experiments (black), and (C) the evolution of the force acting on the lattice versus time; (D) Final stage of indentation on a MT lattice with 12 dimers in each PF and only the minus end of the lattice kept fixed, (E) the distribution of bending angles from this type of simulation (magenta) versus angles obtained during in vitro severing experiments (black), and (F) the evolution of the force acting on the lattice versus time. Data from reference (76).

To probe the proposed "wedge" mechanism of action of severing enzymes on MT filaments described above, we followed the bending and breaking of MT lattices under the action of mechanical forces applied using a constant loading rate regime and through a cantilever sphere that recalls the indentation set-up from AFM experiments (76). To ensure that our results are not influenced by finite-size effects, we probed MT filaments of various lengths. Figure 4 depicts our main findings for the simulation set-ups leading to the two most distinct behaviors.

"The left panels in Figure 4 show our results for a typical run where we considered the "wedge" action on a short interior region of a MT filament. Namely, the cantilever sphere pushed on a short MT lattice resting on a plate and with both ends kept fixed, as depicted in Figure 4A for indentation on the seam of a MT lattice with 8 dimers in each PF (MT8). We found an initial harmonic bending behavior typical of a viscoelastic material at low forces (Figure 4C). Further increase in the applied force to 0.500 nN leads to the breaking of the lateral interactions at the seam, rather than the buckling response seen in covalently linked filaments or in continuous models of biomolecular filaments such as MTs (79-83). Under pushing forces exceeding the 0.600 nN corresponding to the plateau in Figure 4C, we found the breaking of longitudinal interfaces between tubulin subunits. The degree of breaking of the lattice is depicted in the simulation snapshot from Figure 4A. Comparison of the distribution of bending angles for the MT lattice in our simulations with the distribution arising from in vitro severing experiments using katanin p60 (84) (Figure 4B) shows that the two distributions are different. This is confirmed by using the Kolmogorov-Smirnov statistics test, as detailed in our published work (76). Importantly, we found the same behavior in all our simulations for fixed ends lattices, irrespective of the exact pushing location (on the seam, on a PF, away from the seam). We thus concluded that this simulation setup is unlikely to be a good representation of the behavior of MT lattices during in vitro severing. This failure could be due to something as simple as finite-size effects or as serious as the probing of the wrong mechanism. To investigate the first scenario, we probed the mechanics of longer lattices.

"The right panels in Figure 4 show our results for a typical run where we investigated the "wedge" action of a severing enzyme on a longer region of a MT filament with only the minus end fixed, which mimics the presence of the centrosome. The removal of the constraint at the plus-end of the filament in essence allows us to probe the response of a filament longer than 50% compared to the filament from Figure 4A. Namely, the cantilever sphere pushed, as depicted in Figure 4D, on the seam of a MT lattice with 12 dimers in each PF (MT12) with the plus-end kept freely fluctuating. Similar to our above results, we found an initial harmonic bending behavior (Figure 4F). Further increase in the applied force to 0.350 nN leads to the breaking of the lateral interactions keeping PFs 1 and 13 joined at the seam. Unlike our above results for indentation on lattices with both ends fixed, in this time the loss the lateral interface leads to the displacement of these two PFs with respect to each other: one PF gets translated by the length of a full subunit with respect to its former neighbor. Equally important, in this type of simulations we found only very limited breaking of longitudinal interfaces between tubulin subunits occurring only near the fixed minus end of the filament. The degree of breaking of the lattice is depicted in the simulation snapshot from Figure 4D. Comparison of the distribution of bending angles for the MT12 lattice in our simulations with the distribution arising from in vitro severing experiments using katanin p60 (84) (Figure 4E) shows that the two distributions are almost indistinguishable. These results allowed us to conclude that wedging is crucial for the severing of MTs by katanin p60 in in vitro experiments and that it is likely to follow the pathways for radial compression of MTs with the plus end free. For example, we would predict that intermediate conformations populated during the severing of the lattice would correspond to states such as the one depicted in Figure 4D. Indeed, this type of conformation resembles severing intermediates recently found in TEM-based experiments of MT severing (85).

To probe the proposed "unfoldase" mechanism of action of severing enzymes on MT filaments, we followed the bending and breaking of MT lattices of increasing lengths under the action of pulling forces applied using a constant loading rate regime, following the approach detailed in the Methods.

Figure 5 depicts our main findings for the simulations that led to the most distinct responses of the lattice (74).

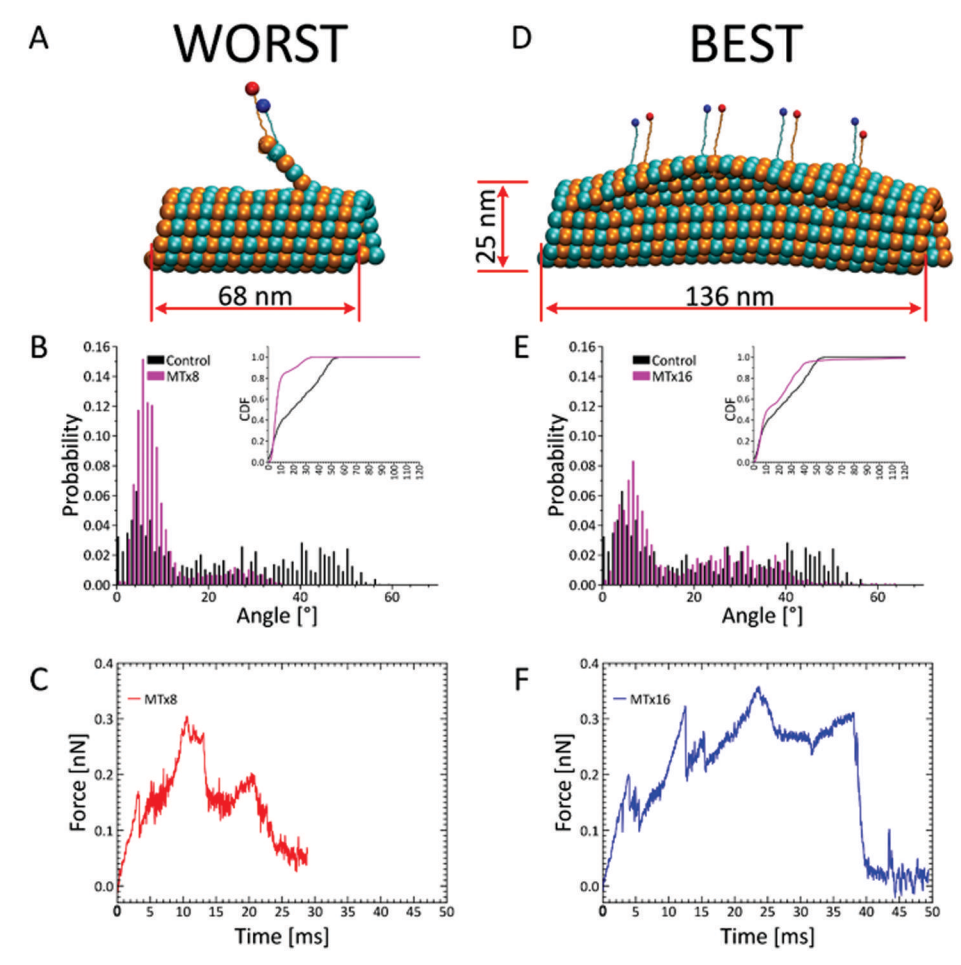


Figure 5. Results of molecular pulling studies of MT lattices. (A) Final stage of pulling on the central subunit from the upper surface of a MT lattice with 8 dimers in each PF and the ends of the lattice kept fixed. The pulled C-terminal ends are depicted as a small red sphere for  $\alpha$ -tubulin and a small blue sphere for  $\beta$ -tubulin. The dimensions of the lattice (filament length and diameter) are listed, (B) the distribution of bending angles from this type of simulation (magenta) versus angles obtained during in vitro severing experiments (black), and (C) the evolution of the force acting on the lattice versus time; (D) Final stage of pulling on the 4 subunits from the top 3 neighboring PFs located on the upper surface of a MT lattice with 16 dimers in each PF and the ends of the lattice kept fixed, (E) the distribution of bending angles from this type of simulation (magenta) versus angles obtained during in vitro severing experiments (black), and (F) the evolution of the force acting on the lattice versus time. Data from reference (74).

The left panels in Figure 5 show our results for a typical run where we modeled the unfoldase mechanism for severing as the action of a single enzyme, which is believed to act only on a single subunit from a MT filament at a time. Namely, following our above work probing the wedge action, we pulled the C-terminal ends of the monomers from a single subunit from a short MT lattice with both ends kept fixed, as depicted in Figure 5A for pulling on the middle dimer on the upper surface of a MT lattice with 8 dimers in each PF (MT8). The first event, corresponding to the first peak

force of 0.150 nN from Figure 5C, was the unraveling of the pulled C-terminal ends. Further increase in the applied force to 0.300 nN leads to the breaking of the contacts between the pulled dimer and its two lateral neighbors. This is closely followed by the loss of the interface between the pulled dimer and one if its two longitudinal neighbors in the PF, leading to the pulling of the resulting PF fragment away from the filament as depicted in Figure 5A. Comparison of the distribution of bending angles for the MT lattice in our simulations with the distribution arising from in vitro severing experiments using katanin p60 (84) (Figure 5B) shows that the two distributions are drastically different. Importantly, unlike for the "wedge" mechanism, we found the same behavior in all our simulations for pulling on a single subunit irrespective of the length of the MT filament and the conditions used for the ends of the filament. The only slight improvement in the agreement between the bending progression in simulations and in severing experiments was when we simulated the pulling of a single subunit next to specific lattice defects (74). We thus concluded that this simulation setup is unlikely to be a good representation of the behavior of MT lattices during in vitro severing. Because, as discussed, we ruled out finite-size effects as a possible explanation for this failure, we had to assume that the failure was likely due to the probing of the wrong mechanism. To investigate an alternative unfoldase scenario, we probed the action of multiple enzymes acting on multiple subunits from a lattice.

The right panels in Figure 5 show our results for a typical run where we modeled the unfoldase mechanism for severing as the concerted action of multiple enzymes, with each severing protein acting on single subunit from a MT filament at a time. In Figure 5D we depict an important intermediate corresponding to the action of 4 severing enzymes acting on 4 tubulin dimers located on 3 neighboring PFs from the upper surface of a MT lattice with 16 dimers in a PF (MT16) with ends fixed. This state corresponds to the unraveling of the pulled C-terminal ends of the 4 dimers and the loss of extensive lateral interfaces in the filament. The forces, per enzyme, required to reach this intermediate reported in Figure 5F are similar in magnitude to the ones obtained for the single enzyme acting alone on a subunit from Figure 5C. Despite of this agreement, the distribution of bending angles experienced by the MT lattice as a result of the concerted action of these 4 enzymes is substantially different from the one above for the single enzyme acting alone. Importantly, as shown in Figure 5E, this new distribution is getting closer to the experimental distribution. Thus, we concluded that if the severing mechanism includes an unfoldase component, then this corresponds to the concerted action of multiple enzymes acting on subunits from neighboring PFs.

#### **Conclusions**

Our simulations of Clp-mediated unfolding and translocation of model SPs indicate the strong effect of local topology near the SP C-terminal (39, 40). Whereas unfolding of both HBP and the  $\alpha/\beta$  protein proceeds from the C-terminal engaged by ClpY and translocation occurs through a power stroke mechanism, we find topology-specific remodeling aspects. Fast unfolding time scales are observed for the  $\alpha$ -helical structure of HBP as a result of the soft mechanical interface probed compared with the longer time scales of the  $\alpha/\beta$  protein that presents a stronger interface. In addition, unfolding pathways are consistent with the mechanical anisotropy properties of the SPs. Clp-mediated remodeling is distinct from bulk mechanical pulling due the ability to apply mechanical force along diverse SP mechanical directions and due to the entropic barrier presented by the narrow central pore. Nevertheless, our simulations of tandem I27 SPs reveal that unfolding in restrained geometries or of multidomain SPs in unrestrained geometries may result in stringent selection of mechanical interfaces probed and corresponding pathways.

Our investigations into the two main proposed MT severing mechanisms revealed that from the fit of the mechanical response of the lattice resulting from simulations to the response from in vitro severing experiments the "wedge" mechanism for relatively long MT lattice fragments is the only one that fully accounts for the experimental findings (76). In contrast, an "unfoldase" mechanism relying on the action of a severing enzyme on a single tubulin subunit at a time is not realistic. Still, our study shows that an "unfoldase" action can be part of the severing mechanism, but only if it corresponds to the concerted action of multiple enzymes acting on subunits located in neighboring PFs (74). A careful investigation into the common factor between the response of a MT filament to the two plausible severing actions, i.e., either to indentation ("wedge") or to multiple point pulling on neighboring PFs ("unfoldase") revealed that in both cases the force application always leads to the bending and breaking of multiple neighboring PFs. This is unlike the pulling action of a single enzyme or of multiple enzymes acting on distant PFs when only the individual pulled PF(s) undergoes bending and breaking. We thus concluded that a requirement for severing is that the mechanism must correspond to the bending and breaking of multiple neighboring PFs.

In summary, our review illustrates the versatility of multiscale simulations in probing SP remodeling mediated by AAA+ nanomachines. Alternative approaches that couple conformational pathways and the effect of local mechanical perturbation of protein structure provide complementary information of these complex mechanisms. For instance, investigation of large–scale conformational transitions of the GroEL chaperonin using an elastic network model–based approach reveals the strong directionality of the generating force applied near the ATP–binding site (86).

### **Computational Methods**

# Simulations of ClpY-Mediated Unfolding and Translocation of Model SPs Coarse-Grained Models of ClpY-SP Systems

Coarse–grained descriptions of the ClpY–SP systems represent each amino acid as a single bead located at the  $C_{\alpha}$  atom position (87). In the studies of the four–helix bundle protein (HBP) (77) and the  $\alpha/\beta$  model proteins, we distinguish three amino acid types, hydrophobic (B), hydrophilic (L), or neutral (N) (88). We use the CHARMM molecular modeling program (89) to perform coarse–grained Langevin dynamics simulations of these systems. Interaction parameters for HBP, which has 73 amino acids and comprises four identical helices connected by three identical loops, were obtained by Guo and Thirumalai (88) and those for the  $\alpha/\beta$  protein, which has 56 amino acids and comprises two  $\beta$ –hairpins and a central  $\alpha/\beta$ –helix, by Sorenson and Head-Gordon (90). The interaction potential is

$$V_{total} = V_{BL} + V_{BA} + V_{DA} + V_{NB} \tag{1}$$

Here, the bond–length potential is  $V_{BL} = \sum 1/2 \, k_b (\sigma - \sigma_0)^2$ , the bond–angle potential is  $V_{BA} = \sum 1/2 \, k_\theta (\theta - \theta_0)^2$  with  $k_b = (100\epsilon_h)/\sigma_0^2$ ,  $\sigma_0 = 3.8 \, \text{Å}$ ,  $k_\theta = 20\epsilon_h rad^{-2}$ ,  $\theta_0 = 105^0$ , and  $\epsilon_h = 1.25 \, \text{kcal/mol}$ . The dihedral angle potential is  $V_{DA} = \sum (A[1+\cos\phi] + B[1-\cos\phi] + C[1+\cos3\phi] + D[1+\cos(\phi+\pi/4)]$ ). We used secondary structure–specific parameters for each SP. For HBP, dihedral angle potentials for helical regions had A = 0,  $B = C = D = 1.6 \, \epsilon_h$  and for turn regions A = B = D = 0 and  $C = 0.2 \, \epsilon_h$ . For the  $\alpha/\beta$  protein, for helical regions A = 0,  $B = C = D = 1.2 \, \epsilon_h$  for turns A = B = D = 0,  $C = 0.2 \, \epsilon_h$  and for  $\beta$ -strands  $A = 0.9 \, \epsilon_h$ ,  $C = 1.2 \, \epsilon_h$ ,  $C = 0.9 \, \epsilon_h$ , C =

is  $V_{NB} = \sum V_{ij} \left( r_{ij} \right) = \sum 4 \, \epsilon_{ij} \left[ \left( \sigma_{ij} / r_{ij} \right)^{12} - \left( \sigma_{ij} / r_{ij} \right)^{6} \right]_{\text{where } r_{ij}}$  is the residue–residue distance. Here,  $\epsilon_{ij} = 2.125$  kcal/mol and  $\sigma_{ij} = 3.8$ Å, for i = j = B,  $\epsilon_{ij} = 10^{-12}$  kcal/mol and  $\sigma_{ij} = 40.47$ Å for  $i = \{L, N\}$  and  $j = \{B, L, N\}$  (effective repulsive interaction) (91). For the  $\alpha/\beta$ protein,  $V_{NB} = \sum 4 \, \epsilon_h S_1 \left[ \left( \sigma_0 / r_{ij} \right)^{12} - S_2 \left( \sigma_0 / r_{ij} \right)^{6} \right]_{\text{with } S_1 = S_2 = 1}$  for BB,  $S_1 = 1/3$ ,  $S_2 = -1$  for BL and LL, and  $S_1 = 1$ ,  $S_2 = 0$  for BN, LN, and NN pairs (90, 92). The C-terminal SsrA peptide tag SsrA (sequence AANDENYALAA) is modeled using turn parameters. Langevin dynamics simulations with a friction coefficient of 1 ps<sup>-1</sup> and time step of 25 fs are performed at T  $\approx 0.7$  T<sub>f</sub> (HBP,  $\alpha/\beta$ ) or T  $\approx 0.9$  T<sub>f</sub> ( $\alpha/\beta$ ), where the folding temperature of HBP ( $\alpha/\beta$ ) is T<sub>f</sub> = 440 (260) K.

#### **ClpY Allostery**

Conformational transitions of ClpY subunits associated with allosteric cycles are modeled using the generalized constant velocity method (91). To this end, ClpY structures corresponding to the "open" and "closed" pore configurations, with Protein Data Bank (PDB) ID 1DO2 and 1DO, respectively (5), are best fitted to minimize their root—mean—square deviation. Each ClpY hemicycle is described through three sequential transitions consisting of two adjacent subunits moving between their conformations in the open and closed pore states and four "inactive" subunits being maintained in fixed conformations. In this approach, each amino acid bead of "active" subunits moves at a constant velocity. In the initial configurations, the HBP–SsrA ( $\alpha/\beta$ –SsrA) SP is located on the proximal side of ClpY, aligned with the pore axis (selected as the z–axis), at a distance of 8 Å from the pore surface. The duration of each simulation trajectory is 50  $\tau$ , where  $\tau$  is the cycle duration. Trajectories that result in partial SP translocation are extended for an additional 70  $\tau$  while including a harmonic restraint with spring constant of k = 0.5 kcal/(mol Ų) and equilibrium length of 6.5 Å for translocated amino acids ( $z - \langle z_{loops} \rangle 14.5$  Å).

#### **ClpY-SP Interaction Potential**

We model interactions between amino acids of ClpY or SsrA and of the folded SP domains by using scaled intra–SP domain interactions such that  $V_{Gi;Hj} = \lambda_{Gi;Hj} \ V_{Hi;Hj}$ , where  $G = \{ClpY, SsrA\}$ ;  $H = \{SsrA, \alpha/\beta, HBP\}$  and  $ij = \{B, L, N\}$ . For the SP we use  $\lambda_{SsrA,HBP} = \lambda_{SsrAB;SsrAB} = 0.25$ ,  $\lambda_{SsrAL,SsrAL} = 1$ . For ClpY we assign  $\lambda_{ClpYB,H} = 2.0$  for hydrophobic amino acids on the distal surface to preclude reversal of SP translocation. For the active subunits, we assign stronger (weaker) interactions,  $\lambda_{ClpYB;H} = 1.5$  (1.0), of central channel loops with the hydrophobic beads of the SP during the closing (opening) transitions. The strength of the ClpY-SP interaction corresponds to a pulling force on the order of 100 pN as determined for the AAA+ motor PilT (93). All other interactions have  $\lambda_{ClpY,H} = 1.25$ .

#### Coarse-Grained Model of ClpY∆I-I27 SP

#### $ClpY\Delta I$ Configurations

We performed coarse-grained simulations using three fixed ClpY $\Delta$ I conformations to represent the open pore and two partially closed pore states. We use the crystal structure with PDB ID 1DO2 to represent the open pore configuration (5). In partially closed states the con-formations of two (four)

subunits are obtained from the crystal structure of the closed pore state with PDB ID 1DO0 (5), whereas the remaining subunits have open-state conformations. ClpY $\Delta$ I is modeled through removal of the auxiliary I-domain (residues 111-242) and the SP consists of I27-(SsrA)<sub>2</sub> (unrestrained geometry) or (SsrA)<sub>2</sub>-I27-(SsrA)<sub>2</sub> (restrained geometry). The native conformation of I27 is obtained from the crystal structure with PDB ID 1TIT (94) and SsrA is described as an unfolded chain.

Interaction Potential of ClpY-I27 SP System

We use the  $C_{\alpha}$  Gō-model developed by Karanicolas-Brooks (KB) (95, 96) to describe I27 interactions. In this model the interaction potential between native pairs is:

$$V_{ij} = \epsilon_{ij} \left[ 13 \left( \sigma_{ij} / r_{ij} \right)^{12} + 18 \left( \sigma_{ij} / r_{ij} \right)^{10} - 4 \left( \sigma_{ij} / r_{ij} \right)^{6} \right]$$
 (2)

with  $r_{ij}$  equal to the distance between particles i and j and  $\sigma_{ij}(-\epsilon_{ij})$  are the distance (energy) of the minimum potential. Inter–molecular and SsrA–I27 or SsrA–SsrA interactions are modeled as repulsive with  $\sigma_{ij}=11.2\,$  Å and  $\epsilon_{ij}=1.32\times10^{-4}\,$  kcal/mol. We use the CHARMM software (89, 97) to perform Langevin dynamics simulations with friction coefficient of 0.1 ps<sup>-1</sup> at T = 0.7 T<sub>f</sub>, where  $T_f=288\,$ K for I27 (98).

### Mechanical Pulling of the SP

Initial SP orientations are prepared by aligning the tandem I27 along the direction of the ClpY $\Delta$ I pore axis and applying successive 45 rotations. Constant velocity pulling is applied at the C–terminal through a harmonic potential. In the restrained geometry, we apply an N– terminal opposing force of 100 pN and a harmonic cylindrical restraint  $C(r) = k_c r^2$  where  $k_c = 100 \text{ kcal/(mol Å}^2)$  is the force constant and r is the axial distance.

#### Implicit Solvent Model Simulations of ClpY∆I-SP

*Initial Configuration of the ClpY\DeltaI-SP System* 

We performed atomistic simulations of the ClpY $\Delta$ I-SP system by using the EEF1 implicit solvent model (99, 100). The implicit solvent approach is computationally efficient and it can access long effective time scales that are relevant for large–scale conformational transitions (101, 102). We also note that EEF1 is a transferable force field which yields results in good agreement with those obtained using explicit solvent representations of the GroEL-rhodanese system (103). SPs comprise tandems of 1, 2, or 4 titin I27 domains and an (SsrA)<sub>2</sub> degradation tag fused at the C–terminal, in the unrestrained geometry, or at each terminal in the restrained geometry. The double–length degradation tag enables us to avoid bias in the initial configuration through the larger separation between ClpY and the I27 domains. In the initial configuration, the multidomain SP is located on the proximal side of ClpY and it is aligned with the direction of the pore axis. The center of mass of ClpY is at the origin and the z axis is parallel to the pore axis such that the distal side is in the positive z direction. The center of mass of the C–terminal I27 domain is located at z  $\approx$  -30 Å and the degradation tag is partially inserted within the ClpY pore. Distinct equilibrated conformations of the multidomain SPs are obtained by performing bulk simulations using the crystal structure of

the human I27 domain with PDB ID 1TIT (94) and a model-built extended conformation of SsrA and are used as initial configurations of simulation trajectories. Random SP rotations about the z axis are applied to the aligned tandem SPs to avoid bias in the polar orientation with respect to the ClpY surface. Our Langevin dynamics simulations were performed at T = 300 K, with a friction coefficient of 5 ps<sup>-1</sup> and a time step of 2 fs using the CHARMM program (97) and XSEDE supercomputer resources (104).

#### Repetitive Cycles of the ClpY $\Delta$ I Machine

Conformational transitions of individual subunits of the ClpYΔI machine are described by using the targeted molecular dynamics (105) approach which involves gradual reduction of the root mean square deviation (rmsd) with respect to the target conformation. This approach yields good results when motions of the nanomachine subunits can be described by a small number of collective variables (CVs), as in the case of the GroEL (106-109). The Clp ATPase cycle comprises twelve sequential transitions of individual subunits in the clockwise direction (as viewed from the proximal side). Each cycle is initiated from a randomly selected subunit and in each step the center of mass of the five inactive subunits is restrained. Transitions of each subunit occur between the open and closed pore conformations, which are described using the Escherichia coli ClpY crystal structures with PDB IDs 1DO2 (open pore) and 1DO0 (closed).<sup>5</sup> In these simulations, the truncated ClpY nanomachine, which lacks the I domains (residues 111–242), is represented by using two chains per subunit. During the active hemicycle we apply an external pulling force, in the positive z direction, on the SP amino acids located within the ClpY. The force is uniformly distributed on the heavy atoms and its magnitude is distributed on a Gaussian with average  $150 \pm 10$  pN in the unrestrained geometry or  $300 \pm 10$  pN in the restrained geometry. The opposing force applied at the N–terminal in the restrained geometry has a constant magnitude of 150 pN.

# Modeling the Mechanical Action of Severing Proteins on Microtubule Lattices

#### The Potential Energy for the SOP Model

We used the self-organized polymer (SOP) model and Brownian dynamics integrated using the Ermak-McCammon algorithm (110) for all our simulation runs probing the response of MT lattices to applied forces (73). Our runs were accelerated on graphics processing units (GPUs) using the gSOP software (versions 1.07 and 2.0) (111). The potential energy function used in the SOP model ( $V_T$ ) is the sum of covalent and non-covalent terms: the finite extensible non-linear elastic ( $V_{FENE}$ ) potential for the covalent bonds, and the Lennard-Jones potential for the non-covalent, non-bonded interactions ( $V_{NB}^{ATT}$  and  $V_{NB}^{REP}$ ).

$$V_{T} = V_{FENE} + V_{NB}^{ATT} + V_{NB}^{REP}$$

$$V_{FENE} = \sum_{i=1}^{N-1} \frac{k}{2} R_{0}^{2} log \left( 1 - \frac{\left( r_{i,i+1} - r_{i,i+1}^{0} \right)^{2}}{R_{0}^{2}} \right)$$

$$V_{NB}^{ATT} = \sum_{i=1}^{N-3} \sum_{j=i+3}^{N} \epsilon_{h} \left[ \left( \frac{r_{i,j}^{0}}{r_{i,j}} \right)^{12} - 2 \left( \frac{r_{i,j}^{0}}{r_{i,j}} \right)^{6} \right] \Delta_{ij}$$

$$V_{NB}^{REP} = \sum_{i=1}^{N-2} \epsilon_{l} \left( \frac{\sigma_{i,i+2}}{r_{i,i+2}} \right)^{6} + \sum_{i=1}^{N-3} \sum_{j=i+3}^{N} \epsilon_{l} \left( \frac{\sigma}{r_{i,j}} \right)^{6} \times (1 - \Delta_{ij})$$
(3)

Here each amino acid is represented by its  $C_{\alpha}$  position,  $\epsilon_h$  is the strength of the native contacts in the lattice, k=20.0 kcal/mol Å<sup>2</sup>,  $R_0=2.0$  Å,  $r_{i;i+1}$  is the 3 dimensional distance between positions i and i + 1 in the chain for i = 1, 2, ..., N, where N is the total number of residues, while  $r_{ij}$  represents the distance between two residues, i and j with  $r_{ij}^{\ 0}$  being its corresponding value in the initial structure. For the non-bonded part of the potential energy, we considered two residues i and j where |i-j|>2 to be in contact if their  $C_{\alpha}$  positions are within a cut-off of  $R_c=8.0$  Å; inside the cutoff distance,  $\Delta_{ij}=1$  and outside it is zero. Finally, we used  $\sigma=3.8$  Å and  $\epsilon_l=1$  kcal/mol.

#### Parameterization of the MT Lattices for the SOP Model

In our simulations we modeled MTs comprised of 13 PFs with varied numbers of dimers per PF (8, 12, and 16) to account for any finite-size effects. We started form a single ring of 13 dimers based on the atomistic structures for sets of PFs (112, 113), which we subsequently duplicated and placed longitudinally, oriented from the  $\alpha$  (minus) to the  $\beta$  (plus) end, until we reached the appropriate dimer length (75, 76, 114).

To determine the contact strength in the Lennard-Jones potential,  $\epsilon_n$ , we used a parametrization approach based on running extensive atomistic molecular dynamics simulations in implicit solvent, which are described in detail in our previous work (75, 114). Consequently, we set  $\epsilon_n$  to 1.9 kcal/mol for the strength of the intra-dimer contacts, 1.0 kcal/mol for the longitudinal contacts, and 0.9 kcal/mol for the lateral contacts. Importantly, as discussed in our prior work (76), we found that these values of the interaction strengths are also in agreement with the results of atomistic simulations in explicit solvent (115). Moreover, we found that the distribution of forces leading to the break and collapse of various MT lattices, modeled using these parameters, under indentation closely resembles the forces reported from AFM experiments carried out on MTs (75, 76, 114).

#### Simulation Setup and Analysis

For the study of pulling on a MT lattice, we applied point forces on selected residue(s) from the C-terminal regions of the monomers from tubulin subunits (the  $\beta$ -tubulin and the  $\alpha$ -tubulin) at a speed of 2.0  $\mu$ m/s, which is the speed used in AFM indentation experiments (69) and thus the speed used in our MT indentation simulations. To study the effect of enzyme concentration in the severing action, we applied forces either to a single tubulin unit or to multiple subunits located on neighboring PFs (see Figure 5A and, respectively, Figure 5D). In the simulations mimicking the concerted action of multiple enzymes, we pulled on multiple subunits from neighboring PFs. We chose the subunits such that they were separated by a distance longer than twice the diameter of the katanin hexamer (53) to mimic a set-up where actual multiple hexameric enzymes have enough space to bind at the same time on the MT lattice. In all simulations, the pulling direction was perpendicular to the long axis (Z-axis) of the MT lattice and away from the outer surface of the filament (74).

For the study of indentation on MT filaments, we used a rigid sphere with radius  $R_{tip}=10$  nm to represent the cantilever. Importantly, the size of the sphere was similar to the diameter of the newly solved structure of the katanin hexamer (53). Following AFM experiments, we set up the pushing simulations such that the cantilever induced fracturing of the MT at a speed of 2.0  $\mu$ m/s (69). For consistency, we used the same speed in our pulling simulations. We ran two types of indentation simulations: one, similar to the AFM set-up, where the MTs rested on a plate, and the second where the MTs were simply held fixed at one or at both ends, to mimic the cytosol. For the indentation runs

we set the interactions between the positions in the MT filament and both the plate and the cantilever to only the repulsive part of the standard Lennard-Jones potential,  $V_{LJ} = \epsilon_{LJ} \left( \sigma_{LR} / (r_i - R_{tip}) \right)^6$ . Here  $\epsilon_{LJ} = 4.18$  kcal/mol,  $\sigma_{LR} = 1.0$  Å is the distance between the center of the sphere representing the tip and an amino acid, and  $r_i$  is position of the i-th particle. The cantilever spring constant was  $k_s = 50$  pN/nm, following the choice from AFM experiments (76).

In our simulations, carried out at 300 K, we used an integration timestep of 40 ps, corresponding to a unitless friction coefficient for an amino acid in water,  $\zeta$ = 50.0. The calculation of the timestep was based on h = 0.16  $\tau_H$  given that  $\tau_h = (\zeta \, \epsilon_h/k_B \, T) \tau_L$  and  $\tau_L = 2.0$  ps as in our previous work (75). We selected frames in our plots corresponding to 40  $\mu$ s. To probe the mechanical response of MT lattices under various conditions of force application and to mimic various experimental conditions, we ran multiple trajectories where we varied the point of contact with the MT lattice, the constraints at the ends of an MT filament, and in the presence or absence of a plate such as the one included in AFM indentation experiments.

For data analysis of the simulation runs we focused on the force versus frames, the force-extension curves, the force-indentation curves, the time evolution of contacts for dimers in a lattice, and the evolution of the bending angles for an MT lattice. Finally, we also compared and contrasted our distributions of bending angles from the pulling and the indentation simulations with the distribution of kinking angles obtained from in vitro severing experiments (74, 76, 84). We use Visual Molecular Dynamics (VMD) (116) for molecular graphics within each figure.

### Acknowledgments

This work has been supported by National Science Foundation (NSF) grants MCB-0845002, MCB-1412183 and MCB-1817948 to R.I.D. and by a grant from the American Heart Association and NSF grants MCB-0952082 and MCB-1516918 to G.S. This work used the Extreme Science and Engineering Discovery Environment (XSEDE), which is supported by NSF grant number ACI-1548562. XSEDE Comet resources were used at the San Diego Supercomputer Center through allocation TG-MCB170020 to G.S.

#### References

- 1. Hanson, P. I.; Whiteheart, S. W. AAA+ proteins: have engine, will work. *Nat. Rev. Mol. Cell Biol.* **2005**, *6*, 519–529.
- 2. Enemark, E. J.; Joshua-Tor, L. On helicases and other motor proteins. *Curr. Opin. Struct. Biol.* **2008**, *18*, 243–257.
- 3. Sauer, R. T.; Baker, T. A. AAA+ Proteases: ATP-Fueled Machines of Protein Destruction. *Annu. Rev. Biochem.* **2011**, *80*, 587–612.
- 4. Weber-Ban, E. U.; Reid, B. G.; Miranker, A. D.; Horwich, A. L. Global unfolding of a substrate protein by the Hsp100 chaperone ClpA. *Nature* **1999**, *401*, 90–93.
- 5. Bochtler, M.; Hartmann, C.; Song, H. K.; Bourenkov, G. P.; Bartunik, H. D.; Huber, R. The structures of HslU and the ATP-dependent protease HslU-HslV. *Nature* **2000**, *403*, 800–805.
- Sousa, M. C.; Trame, C. B.; Tsuruta, H.; Wilbanks, S. M.; Reddy, V. S.; McKay, D. B. Crystal and Solution Structures of an HslUV Protease-Chaperone Complex. *Cell* 2000, 103, 633–643.

- Hoskins, J. R.; Singh, S. K.; Maurizi, M. R.; Wickner, S. Protein binding and unfolding by the chaperone ClpA and degradation by the protease ClpAP. *Proc. Natl. Acad. Sci. USA* 2000, 97, 8892–8897.
- 8. Kessel, M.; Wu, W.-F.; Gottesman, S.; Kocsis, E.; Steven, A.; Maurizi, M. Six-fold rotational symmetry of ClpQ, the E. coli homolog of the 20S proteasome, and its ATP-dependent activator, ClpY. *FEBS Lett.* **1996**, 398, 274–278.
- 9. Ogura, T.; Wilkinson, A. AAA+ superfamily ATPases: common structure–diverse function. *Genes to Cells* **2001**, *6*, 575–597.
- Song, H.; Hartmann, C.; Ramachandran, R.; Bochtler, M.; Behrendt, R.; Moroder, L.; Huber, R. Mutational studies on HslU and its docking mode with HslV. *Proc. Natl. Acad. Sci. USA* 2000, 97, 14103–14108.
- 11. DeLaBarre, B.; Brunger, A. T. Nucleotide dependent motion and mechanism of action of p97/VCP. *J. Mol. Biol.* **2005**, 347, 437–452.
- 12. Weibezahn, J.; Schlieker, C.; Bukau, B.; Mogk, A. Characterization of a trap mutant of the AAA+ chaperone ClpB. *J. Biol. Chem.* **2003**, 278, 32608–17.
- 13. Martin, A.; Baker, T. A.; Sauer, R. T. Protein unfolding by a AAA+ protease is dependent on ATP-hydrolysis rates and substrate energy landscapes. *Nat. Struct. Mol. Biol.* **2008**, *15*, 139–145.
- 14. Martin, A.; Baker, T.; Sauer, R. Diverse pore loops of the AAA plus ClpX machine mediate unassisted and adaptor-dependent recognition of ssrA-tagged substrates. *Mol. Cell* **2008**, 29, 441–450.
- 15. Siddiqui, S. M.; Sauer, R. T.; Baker, T. A. Role of the processing pore of the ClpX AAA+ ATPase in the recognition and engagement of specific protein substrates. *Genes Dev.* **2004**, *18*, 369–374.
- 16. Guo, F.; Maurizi, M.; Esser, L.; Xia, D. Crystal structure of ClpA, an Hsp100 chaperone and regulator of ClpAP protease. *J. Biol. Chem.* **2002**, 277, 46743–46752.
- 17. Kim, D. Y.; Kim, K. K. Crystal Structure of ClpX Molecular Chaperone from Heli-cobacter pylori. *J. Biol. Chem.* **2003**, 278, 50664–50670.
- 18. Rohrwild, M.; Pfeifer, G.; Santarius, U.; Muller, S. A.; Huang, H.-C.; Engel, A.; Baumeister, W.; Goldberg, A. L. The ATP-dependent HslVU protease from Es-cherichia coli is a four-ring structure resembling the proteasome. *Nat. Struct. Mol. Biol.* **1997**, *4*, 133–139.
- 19. Ishikawa, T.; Maurizi, M. R.; Belnap, D.; Steven, A. C. ATP-dependent proteases: Docking of components in a bacterial complex. *Nature* **2000**, *408*, 667–668.
- Wojtkowiak, D.; Georgopoulos, C.; Zylicz, M. Isolation and Characterization of ClpX, a New ATP-Dependent Specificity Component of the Clp Protease of Escherichia Coli. *J. Biol. Chem.* 1993, 268, 22609–22617.
- 21. Gottesman, S.; Roche, E.; Zhou, Y.; Sauer, R. The ClpXP and ClpAP proteases degrade proteins with carboxy-terminal peptide tails added by the SsrA-tagging system. *Genes Dev.* **1998**, *12*, 1338–1347.
- 22. Flynn, J. M.; Neher, S. B.; Kim, Y.; Sauer, R. T.; Baker, T. A. Proteomic Discovery of Cellular Substrates of the ClpXP Protease Reveals Five Classes of ClpX-Recognition Signals. *Mol. Cell* **2003**, *11*, 671–683.

- Camberg, J. L.; Hoskins, J. R.; Wickner, S. ClpXP protease degrades the cytoskeletal protein, FtsZ, and modulates FtsZ polymer dynamics. *Proc. Natl. Acad. Sci. USA* 2009, 106, 10614–10619.
- 24. Gottesman, S.; Clark, W.; Maurizi, M. The ATP-dependent Clp protease of Escherichia coli. Sequence of clpA and identification of a Clp-specific substrate. *J. Biol. Chem.* **1990**, 265, 7886–7893.
- 25. Levchenko, I.; Yamauchi, M.; Baker, T. A. ClpX and MuB interact with overlapping regions of Mu transposase: implications for control of the transposition pathway. *Genes Dev.* **1997**, *11*, 1561–1572.
- Hoskins, J. R.; Kim, S.-Y.; Wickner, S. Substrate Recognition by the ClpA Chaperone Component of ClpAP Protease. J. Biol. Chem. 2000, 275, 35361–35367.
- Lee, C.; Schwartz, M. P.; Prakash, S.; Iwakura, M.; Matouschek, A. ATP-Dependent Proteases Degrade Their Substrates by Processively Unraveling Them from the Degradation Signal. *Mol. Cell* 2001, 7, 627–637.
- Kenniston, J. A.; Baker, T. A.; Fernandez, J. M.; Sauer, R. T. Linkage between ATP Consumption and Mechanical Unfolding during the Protein Processing Reactions of an AAA+ Degradation Machine. Cell 2003, 114, 511–520.
- 29. Aubin-Tam, M.-E.; Olivares, A.; Sauer, R.; Baker, T.; Lang, M. Single-Molecule Protein Unfolding and Translocation by an ATP-Fueled Proteolytic Machine. *Cell* **2011**, *145*, 257–267.
- Maillard, R.; Chistol, G.; Sen, M.; Righini, M.; Tan, J.; Kaiser, C. M.; Hodges, C.; Martin, A.; Bustamante, C. ClpX(P) Generates Mechanical Force to Unfold and Translocate Its Protein Substrates. *Cell* 2011, 145, 459–469.
- 31. Sen, M.; Maillard, R.; Nyquist, K.; Rodriguez-Aliaga, P.; Pressé, S.; Martin, A.; Bustamante, C. The ClpXP Protease Unfolds Substrates Using a Constant Rate of Pulling but Different Gears. *Cell* **2013**, *155*, 636–646.
- 32. Cordova, J.; Olivares, A.; Shin, Y.; Stinson, B.; Calmat, S.; Schmitz, K.; Aubin-Tam, M.-E.; Baker, T.; Lang, M.; Sauer, R. Stochastic but Highly Coordinated Protein Unfolding and Translocation by the ClpXP Proteolytic Machine. *Cell* **2014**, *158*, 647–658.
- 33. Olivares, A. O.; Nager, A. R.; Iosefson, O.; Sauer, R. T.; Baker, T. A. Mechanochemical basis of protein degradation by a double-ring AAA+ machine. *Nat. Struct. Mol. Biol.* **2014**, *21*, 871–875.
- 34. Olivares, A. O.; Kotamarthi, H. C.; Stein, B. J.; Sauer, R. T.; Baker, T. A. Effect of directional pulling on mechanical protein degradation by ATP-dependent proteolytic machines. *Proc. Natl. Acad. Sci. USA* **2017**, *114*, E6306–E6313.
- 35. Huang, L.; Kirmizialtin, S.; Makarov, D. E. Computer simulations of the translocation and unfolding of a protein pulled mechanically through a pore. *J. Chem. Phys.* **2005**, *123*, 124903.
- 36. West, D. K.; Brockwell, D. J.; Paci, E. Prediction of the Translocation Kinetics of a Protein from Its Mechanical Properties. *Biophys. J.* **2006**, *91*, L51–L53.
- 37. Wojciechowski, M.; Szymczak, P.; Carrión-Vázquez, M.; Cieplak, M. Protein Unfolding by Biological Unfoldases: Insights from Modeling. *Biophys. J.* **2014**, *107*, 1661–1668.
- 38. Luan, B.; Huynh, T.; Li, J.; Zhou, R. Nanomechanics of Protein Unfolding Outside a Generic Nanopore. *ACS Nano* **2016**, *10*, 317–323.

- 39. Kravats, A.; Jayasinghe, M.; Stan, G. Unfolding and translocation pathway of sub-strate protein controlled by structure in repetitive allosteric cycles of the ClpY ATPase. *Proc. Natl. Acad. Sci. USA* **2011**, *108*, 2234–2239.
- Kravats, A. N.; Tonddast-Navaei, S.; Bucher, R. J.; Stan, G. Asymmetric processing of a substrate protein in sequential allosteric cycles of AAA+ nanomachines. *J. Chem. Phys.* 2013, 139, 121921.
- 41. Tonddast-Navaei, S.; Stan, G. Mechanism of Transient Binding and Release of Substrate Protein during the Allosteric Cycle of the p97 Nanomachine. *J. Am. Chem. Soc.* **2013**, *135*, 14627–14636.
- 42. Kravats, A. N.; Tonddast-Navaei, S.; Stan, G. Coarse-Grained Simulations of Topology-Dependent Mechanisms of Protein Unfolding and Translocation Mediated by ClpY ATPase Nanomachines. *PLoS Comput. Biol.* **2016**, *12*, e1004675.
- 43. Javidialesaadi, A.; Stan, G. Asymmetric Conformational Transitions in AAA+ Biological Nanomachines Modulate Direction-Dependent Substrate Protein Unfolding Mechanisms. *J. Phys. Chem. B* **2017**, *121*, 7108–7121.
- 44. Javidialesaadi, A.; Flournoy, S. M.; Stan, G. Role of Diffusion in Unfolding and Translocation of Multidomain Titin I27 Substrates by a Clp ATPase Nanomachine. *J. Phys. Chem. B* **2019**, 123, 2623–2635.
- 45. Hartman, J. J.; Mahr, J.; McNally, K.; Okawa, K.; Iwamatsu, A.; Thomas, S.; Cheesman, S.; Heuser, J.; Vale, R. D.; McNally, F. J. Katanin, a microtubule-severing protein, is a novel AAA ATPase that targets to the centrosome using a WD40-containing subunit. *Cell* **1998**, 93, 277–287.
- 46. Evans, K. J.; Gomes, E. R.; Reisenweber, S. M.; Gundersen, G. G.; Lauring, B. P. Linking axonal degeneration to microtubule remodeling by spastin-mediated microtubule severing. *J. Cell Biol.* **2005**, *168*, 599–606.
- Zhang, D.; Grode, K. D.; Stewman, S. F.; Diaz-Valencia, J. D.; Liebling, E.; Rath, U.; Riera, T.; Currie, J. D.; Buster, D. W.; Asenjo, A. B.; Sosa, H. J.; Ross, J. L.; Ma, A.; Rogers, S. L.; Sharp, D. J. Drosophila katanin is a microtubule depolymerase that regulates cortical-microtubule plus-end interactions and cell migration. *Nat. Cell. Biol.* 2011, 13, 361–369.
- 48. Roll-Mecak, A.; McNally, F. J. Microtubule-severing enzymes. *Cur. Op. Cell. Biol.* **2010**, 22, 96–103.
- 49. Zhang, D.; Grode, K. D.; Sharp, D. J. Drosophila katanin is a microtubule depolymerase that regulates cortical-microtubule plus-end interactions and cell migration. *Nat. Cell Biol.* **2011**, 13, 361–370.
- 50. Roll-Mecak, A.; Vale, R. D. Structural basis of microtubulue severing by the hereditary spastic paraplegia protein spastin. *Nature* **2008**, *451*, 363–368.
- 51. Yang, D.; Rismanchi, N.; Renvoise, B.; Lippincott-Schwartz, J.; Blackstone, C.; Hurley, J. H. Structural basis for midbody targeting of spastin by the ESCRT-III protein CHMP1B. *Nat, Struct. Mol. Biol.* **2008**, *15*, 1278–1286.
- 52. Hartman, J. J.; Vale, R. D. Microtubule disassembly by ATP-dependent oligomerization of the AAA enzyme katanin. *Science* **1999**, 286, 782–785.

- 53. Zehr, E.; Szyk, A.; Piszczek, G.; Szczesna, E.; Zuo, X.; Roll-Mecak, A. Katanin spiral and ring structures shed light on power stroke for microtubule severing. *Nat. Struct. Mol. Biol.* **2017**, 24, 717–722.
- 54. Nithianantham, S.; McNally, F. J.; Al-Bassam, J. Structural basis for disassembly of katanin heterododecamers. *J. Biol. Chem.* **2018**, 293, 10590–10605.
- 55. Sandate, C. R.; Szyk, A.; Zehr, E. A.; Lander, G. C.; Roll-Mecak, A. An allosteric network in spastin couples multiple activities required for microtubule severing. *Nat. Struct. Mol. Biol.* **2019**, *26*, 671–678.
- 56. Zehr, E. A.; Szyk, A.; Szczesna, E.; Roll-Mecak, A. Katanin Grips the beta-Tubulin Tail through an Electropositive Double Spiral to Sever Microtubules. *Dev. Cell* **2020**, *52*, 118–131.
- Han, H.; Schubert, H. L.; McCullough, J.; Monroe, N.; Purdy, M. D.; Yeager, M.; Sundquist, W. I.; Hill, C. P. Structure of spastin bound to a glutamate-rich peptide implies a hand-overhand mechanism of substrate translocation. *J. Biol. Chem.* 2020, 295, 435–443.
- 58. White, S. R.; Evans, K. J.; Lary, J.; Cole, J. L.; Lauring, B. Recognition of C-terminal Amino Acids in Tubulin by Pore Loops in Spastin is Important for Microtubule Severing. *J. Cell Biol.* **2007**, *176*, 995–1005.
- Davis, L. J.; Odde, D. J.; Block, S. M.; Gross, S. P. The importance of lattice defects in kataninmediated microtubule severing in vitro. *Biophys. J.* 2002, 82, 2916–2927.
- 60. Diaz-Valencia, J.; Morelli, M.; Bailey, M.; Zhang, D.; Sharp, D.; Ross, J. L. Drosophila Katanin-60 Depolymerizes and Severs at Microtubule Defects. *Biophys. J.* **2011**, *100*, 2440–2449.
- Schaap, I. A. T.; dePablo, P. J.; Schmidt, C. F. Resolving the molecular structure of microtubules under physiological conditions with scanning force microscopy. *Eur. Biophys J.* 2004, 33, 462–467.
- 62. Schaedel, L.; John, K.; Gaillard, J.; Nachury, M. V.; Blanchoin, L.; Thery, M. Microtubules self-repair in response to mechanical stress. *Nature Mat.* **2015**, *14*, 1156–1163.
- 63. Eckert, T.; Le, D. T.-V.; Link, S.; Friedmann, L.; Woehlke, G. Spastin's Microtubule-Binding Properties and Comparison to Katanin. *PLoS ONE* **2012**, *7*, e50161.
- 64. Bailey, M. E.; Jiang, N.; Dima, R. I.; Ross, J. L. Microtubule Severing Enzymes Couple ATPase Activity with Tubulin GTPase Spring Loading. *Biopolymers* **2016**, *105*, 547–556.
- 65. Johjima, A.; Noi, K.; Nishikori, S.; Ogi, H.; Esaki, M.; Ogura, T. Microtubule Severing by Katanin p60 AAA+ ATPase Requires the C-terminal Acidic Trails of Both  $\alpha$  and  $\beta$ -Tubulins and Basic Amino Acid Residues in the AAA + Ring Pore. *J. Biol. Chem.* **2015**, 290, 11762–11770.
- 66. McNally, F.; Vale, R. Identification of Katanin, an ATPase That Severs and Disassembles Stable Microtubules. *Cell* **1993**, 75, 419–429.
- 67. Sharp, D.; Ross, J. Microtubule Severing Enzymes at the Cutting Edge. *J. Cell Sci.* **2012**, 125, 2561–2569.
- 68. Barsegov, V.; Ross, J. L.; Dima, R. I. Dynamics of microtubules: highlights of recent computational and experimental investigations. *J. Phys. Cond. Matt.* **2017**, 29, 433003.
- 69. dePablo, P. J.; Schaap, I. A. T.; MacKintosh, F. C.; Schmidt, C. F. Deformation and collapse of microtubules on the nanometer scale. *Phys. Rev. Lett.* **2003**, *91*, 098101.

- Schaap, I. A. T.; Carrasco, C.; dePablo, P. J.; MacKintosh, F. C.; Schmidt, C. F. Elastic response, buckling, and instability of microtubules under radial indentation. *Biophys. J.* 2006, 91, 1521–1531.
- Munson, K. M.; Mulugeta, P. G.; Donhauser, Z. J. Enhanced Mechanical Stability of Microtubules Polymerized with a Slowly Hydrolyzable Nucleotide Analogue. J. Phys. Chem. B Lett. 2007, 111, 5053–5057.
- 72. Donhauser, Z. J.; Jobs, W. B.; Binka, E. C. Mechanics of Microtubules: Effects of Protofilament Orientation. *Biophys. J.* **2010**, *99*, 1668–1675.
- 73. Hyeon, C.; Dima, R. I.; Thirumalai, D. Pathways and kinetic barriers in mechanical unfolding and refolding of RNA and proteins. *Structure* **2006**, *14*, 1633–1645.
- Varikoti, R. A.; Macke, A. C.; Speck, V.; Ross, J. L.; Dima, R. I. Molecular Investigations into the Unfoldase Action of Severing Enzymes on Microtubules. *Cytoskeleton* 2020in press, doi: 10.1002/cm.21606.
- 75. Jiang, N.; Bailey, M.; Burke, J.; Ross, J. L.; Dima, R. I. Modeling the effects of lattice defects on microtubule breaking and healing. *Cytoskeleton* **2017**, *74*, 3–17.
- Szatkowski, L.; Merz, D. E.; Jiang, N.; Ejikeme, I.; Belonogov, L.; Ross, J. L.; Dima, R. I. Mechanics of the Microtubule Seam Interface Probed by Molecular Simulations and in Vitro Severing Experiments. J. Phys. Chem. B 2019, 123, 4888–4900.
- 77. Ho, S. P.; DeGrado, W. F. Design of a 4-helix bundle protein: synthesis of peptides which self-associate into a helical protein. *J. Am. Chem. Soc.* **1987**, *109*, 6751–6758.
- 78. Kenniston, J. A.; Baker, T. A.; Sauer, R. T. Partitioning between unfolding and release of native domains during ClpXP degradation determines substrate selectivity and partial processing. *Proc. Natl. Acad. Sci. USA* **2005**, *102*, 1390–1395.
- 79. Wang, C. Y.; Ru, C. Q.; Mioduchowski, A. Orthotropic elastic shell model for buckling of microtubules. *Phys. Rev. E* **2006**, 74, 052901.
- 80. Vaziri, A.; Mahadevan, L. Localized and extended deformations of elastic shells. *Proc. Natl. Acad. Sci. USA* **2008**, *105*, 7913–7918.
- 81. Yi, L.; Chang, T.; Ru, C. Q. Buckling of microtubules under bending and torsion. *J. Appl. Phys.* **2008**, *103*, 103516.
- 82. Zhang, J.; Meguid, S. A. Buckling of microtubules: An insight by molecular and continuum mechanics. *Appl. Phys. Lett.* **2014**, *105*, 173704.
- 83. Memet, E.; Hilitski, F.; Morris, M. A.; Schwenger, W. J.; Dogic, Z.; Mahadevan, L. Microtubules soften due to cross-sectional flattening. *eLife* **2018**, 7, e34695.
- 84. Harris, B. J.; Ross, J. L.; Hawkins, T. L. Microtubule seams are not mechanically weak defects. *Phys. Rev. E* **2018**, *97*, 062408.
- 85. Vemu, A.; Szczesna, E.; Zehr, E. A.; Spector, J. O.; Grigorieff, N.; Deaconescu, A. M.; Roll-Mecak, A. Severing enzymes amplify microtubule arrays through lattice GTP-tubulin incorporation. *Science* **2018**, *361*, eaau1504.
- 86. Liu, J.; Sankar, K.; Wang, Y.; Jia, K.; Jernigan, R. L. Directional Force Originating from ATP Hydrolysis Drives the GroEL Conformational Change. *Biophys. J.* **2017**, *112*, 1561–1570.
- 87. Honeycutt, J. D.; Thirumalai, D. The nature of folded states of globular proteins. *Biopolymers* **1992**, 32, 695–709.

- 88. Guo, Z.; Thirumalai, D. Kinetics and Thermodynamics of Folding of a de Novo Designed Four helix Bundle Protein. *J. Mol. Biol.* **1996**, *263*, 323–343.
- Brooks, B. R.; Bruccoleri, R. E.; Olafson, B. D.; States, D. J.; Swaminathan, S.; Karplus, M. CHARMM: A Program for Macromolecular Energy, Minimization and Dynamics Calculations. J. Comp. Chem. 1983, 4, 187–217.
- Sorenson, J. M.; Head-Gordon, T. Matching Simulation and Experiment: A New Simplified Model for Simulating Protein Folding. J. Comput. Biol. 2000, 7, 469–481.
- 91. Stan, G.; Lorimer, G. H.; Thirumalai, D.; Brooks, B. R. Coupling between allosteric transitions in GroEL and assisted folding of a substrate protein. *Proc. Natl. Acad. Sci. USA* **2007**, *104*, 8803–8808.
- Brown, S.; Fawzi, N.; Head-Gordon, T. Coarse-grained sequences for protein folding and design. Proc. Natl. Acad. Sci. USA 2003, 100, 10712–10717.
- 93. Maier, B.; Potter, L.; So, M.; Seifert, H. S.; Sheetz, M. P. Single pilus motor forces exceed 100 pN. *Proc. Natl. Acad. Sci. USA* **2002**, *99*, 16012–16017.
- 94. Improta, S.; Politou, A. S.; Pastore, A. Immunoglobulin-Like Modules from Titin I-Band: Extensible Components of Muscle Elasticity. *Structure* **1996**, *4*, 323–337.
- 95. Karanicolas, J.; Brooks, C. L., III The origins of asymmetry in the folding transition states of protein L and protein G. *Prot. Sci.* **2002**, *11*, 2351–2361.
- 96. Karanicolas, J.; Brooks, C. L., III Improved Gō-like models demonstrate the robustness of protein folding mechanisms towards non-native interactions. *J. Mol. Biol.* **2003**, *334*, 309–325.
- 97. Brooks, B. R.; Brooks, C. L.; Mackerell, A. D.; Nilsson, L.; Petrella, R. J.; Roux, B.; Won, Y.; Archontis, G.; Bartels, C.; Boresch, S.; A Caflisch, A.; Caves, L.; Cui, Q.; Dinner, A. R.; Feig, M.; Fischer, S.; Gao, J.; Hodoscek, M.; Im, W.; Kuczera, K.; Lazaridis, T.; Ma, J.; Ovchinnikov, V.; Paci, E.; Pastor, R. W.; Post, C. B.; Pu, J. Z.; Schaefer, M.; Tidor, B.; Venable, R. M.; Woodcock, H. L.; Wu, X.; Yang, W.; York, D. M.; Karplus, M. CHARMM: the biomolecular simulation program. *J. Comp. Chem.* 2009, 30, 1545–1614.
- 98. West, D.; Olmsted, P.; Paci, E. Mechanical unfolding revisited through a simple but realistic model. *J. Chem. Phys.* **2006**, *124*, 154909.
- 99. Lazaridis, T.; Karplus, M. Effective Energy Function for Proteins in Solution. *Proteins: Struct. Func. Genet.* **1999**, 35, 133–152.
- 100. Masunov, A.; Lazaridis, T. Potentials of mean force between ionizable amino acid side chains in water. *J. Am. Chem. Soc.* **2003**, *125*, 1722–1730.
- 101. Anandakrishnan, R.; Drozdetski, A.; Walker, R. C.; Onufriev, A. V. Speed of conformational change: comparing explicit and implicit solvent molecular dynamics simula-tions. *Biophys. J.* **2015**, *108*, 1153–1164.
- 102. Zhang, J.; Lazaridis, T. Calculating the free energy of association of transmembrane helices. *Biophys. J.* **2006**, *91*, 1710–1723.
- 103. van der Vaart, A.; Ma, J.; Karplus, M. The Unfolding Action of GroEL on a Protein Substrate. *Biophys. J.* **2004**, 87, 562–573.
- 104. Towns, J.; Cockerill, T.; Dahan, M.; Foster, I.; Gaither, K.; Grimshaw, A.; Hazlewood, V.; Lathrop, S.; Lifka, D.; Peterson, G. D.; Roskies, R.; Scott, J. R.; Wilkins-Diehr, N. XSEDE: Accelerating Scientific Discovery. *Computing in Science & Engineering* **2014**, *16*, 62–74.

- 105. Schlitter, J.; Engels, M.; Kruger, P.; Jacoby, E. U.; Wollmer, A. Targeted molecular dynamics simulation of conformational change: application to the T-R transition in insulin. *Mol. Sim.* **1993**, *10*, 291–308.
- 106. Keskin, O.; Bahar, I.; Flatow, D.; Covell, D. G.; Jernigan, R. L. Molecular Mechanisms of Chaperonin GroEL-GroES Function. *Biochemistry* 2002, 41, 491–501.
- 107. Zheng, W.; Brooks, B. R.; Thirumalai, D. Allosteric transitions in the chaperonin GroEL are captured by a dominant normal mode that is most robust to sequence variations. *Biophys. J.* **2007**, 93, 2289–2299.
- 108. Tehver, R.; Chen, J.; Thirumalai, D. Allostery Wiring Diagrams in the Transitions that Drive the GroEL Reaction Cycle. *J. Mol. Biol.* **2009**, 387, 390–406.
- 109. Skjaerven, L.; Grant, B.; Muga, A.; Teigen, K.; McCammon, J. A.; Reuter, N.; Martinez, A. Conformational sampling and nucleotide-dependent transitions of the GroEL subunit probed by unbiased molecular dynamics simulations. *PLoS Comput. Biol.* 2011, 7, 1002004.
- 110. Ermak, D. L.; McCammon, J. A. Brownian dynamics with hydrodynamic interactions. *J. Chem. Phys.* **1978**, *69*, 1352–1356.
- 111. Zhmurov, A.; Dima, R. I.; Kholodov, Y.; Barsegov, V. SOP-GPU: Accelerating Biomolecular Simulations in the Centisecond Timescale using Graphics Processors. *Proteins* **2010**, 78, 2984–2999.
- 112. Wells, D. B.; Aksimentiev, A. Mechanical Properties of a Complete Microtubule Revealed through Molecular Dynamics Simulation. *Biophys. J.* **2010**, *99*, 629–637.
- 113. Nogales, E.; Whittaker, M.; Milligan, R. A.; Downing, K. H. High-Resolution Model of the Microtubule. *Cell* **1999**, *96*, 79–88.
- 114. Kononova, O.; Kholodov, Y.; Theisen, K. E.; Marx, K. A.; Dima, R. I.; Ataullakhanov, F. I.; Grishchuk, E. L.; Barsegov, V. Tubulin bond energies and micro-tubule biomechanics determined from nano-indentation in silico. *J. Am. Chem. Soc.* 2014, 136, 17036–17045.
- 115. Ayoub, A. T.; Klobukowski, M.; Tuszynski, J. A. Detailed Per-residue Energetic Analysis Explains the Driving Force for Microtubule Disassembly. *PLoS Comput. Biol.* **2015**, *11*, 1–21.
- 116. Humphrey, W.; Dalke, A.; Schulten, K. VMD Visual Molecular Dynamics. *J. Mol. Graphics* **1996**, *14*, 33–38.